Communications Materials

https://doi.org/10.1038/s43246-026-01102-3

Article in Press

Low stress grain boundary mediated plasticity and early fracture at basal twist grain boundaries in a titanium alloy

Received: 9 September 2025

Accepted: 29 January 2026

Cite this article as: Yvinec, T., Iabbaden, D., Hamon, F. *et al.* Low stress grain boundary mediated plasticity and early fracture at basal twist grain boundaries in a titanium alloy. *Commun Mater* (2026). https://doi.org/10.1038/s43246-026-01102-3

Thomas Yvinec, Djafar Iabbaden, Florence Hamon, Valéry Valle, Julien Guénolé & Samuel Hémery

Low stress grain boundary mediated plasticity and early fracture at basal twist grain boundaries in a titanium alloy

Thomas Yvinec,[1] Djafar Iabadden,[2] Florence Hamon,[1] Valéry Valle,[1] Julien Guénolé[2,*], Samuel Hémery,[1,#]

[1] Institut Pprime, ISAE-ENSMA, Université de Poitiers, CNRS UPR 3346, Téléport 2, 1 avenue Clément Ader, BP 40109, Futuroscope-Chasseneuil Cedex, 86961 France

[2] CNRS, Université de Lorraine, Arts et Métiers ParisTech, LEM3, 57070 Metz, France

[*] julien.guenole@cnrs.fr

[#] samuel.hemery@ensma.fr

Abstract

Titanium alloys are high-performance materials critical for demanding applications in aerospace, defense, and energy sectors. Basal twist grain boundaries were recently identified as key microstructure configurations leading to failures under different conditions. In the present study, we examined deformation and fracture in these specific locations to shed light on the mechanical behavior in relation to grain boundary characteristics. In situ characterization using high resolution digital image correlation was employed, and revealed both unexpectedly low stress deformation and early cleavage-like fracture. The collected dataset enabled the identification of influential grain boundary parameters, including their twist and tilt components. Molecular dynamics simulations of bicrystals subjected to shear loadings properly replicated experimental observations, and unveiled underlying mechanisms. The clarified influence of grain boundary characteristics on the mechanical response offers a new understanding of the detrimental role of basal twist grain boundaries on the performance of titanium alloys.

Introduction

Titanium alloys are key materials for applications requiring lightweight, superior mechanical properties, and excellent corrosion resistance [1]. As a consequence, they are extensively employed in the aerospace industry [2,3]. The Ti-6Al-4V alloy established as the most widely used shortly after its development in the early 1950s [1,4]. The good balance of properties is a major cause of its success, alongside intensive development and testing [4,5]. In particular, the fatigue performance is an important design criterion for many aero-engine and airframe components. The microstructural features are of utmost importance and govern crack initiation, as no pore or inclusion is generally present in aerospace quality materials [1]. Therefore, continuous research efforts aimed at accurate predictions of lifetimes using microstructure sensitive approaches [6–9]. In this context, experimental evidence of underlying mechanisms is a key milestone to develop physically-based modeling.

Despite decades long research efforts, mechanisms governing the initiation of fatigue cracks in titanium alloys have remained the subject of debates, and on-going research efforts. Prior studies clarified numerous features of importance, such as the type of microstructural element [10–12], the crystallographic orientation [12–15], and the crack plane [13,16,17]. Basal twist grain boundaries (BTGB) were identified recently as critical for crack nucleation [18]. This microstructure configuration is composed of two α crystals misoriented about $[0001]$, and separated by an α/α grain boundary (GB) parallel to (0001). No detectable segregation of alloying elements was evidenced at these α/α GBs [19]. Early cracks were found located at BTGBs in various titanium alloys with different microstructures subjected to low-cycle fatigue [18,19]. They were later identified at main crack initiation sites for a variety of loading conditions including high-cycle fatigue, low-cycle fatigue and dwell-fatigue [20–22]. These investigations support limited influences of alloy composition, microstructural characteristics, and mechanical loading conditions,

including the strain rate, on BTGB cracking. The analysis of secondary cracks confirmed the importance of BTGBs [23–25]. However, it often highlights a competition with other mechanisms, such as crack formation along basal or prismatic slip bands. BTGBs prone to early crack nucleation typically correspond to a few instances per squared millimeter in engineering microstructures [26]. This feature was related to the high fatigue lifetime variability noticed in α+β titanium alloys, as it implies a low density of possible crack initiation sites [26].

Limited information is available about the mechanical behavior of BTGBs, although this characteristic is of utmost importance to understand deformation and fracture mechanisms. A recent study highlighted early deformation occurring at these microstructure configurations, as compared to classical slip activity [19]. Additional investigations revealed that the shear is accommodated by the BTGB, without dislocation activity in the adjacent α grains [19]. While the critical resolved shear stresses (CRSS) of the different deformation modes in α-Ti have been extensively characterized [27–33], the threshold stress associated with shearing along BTGBs is not documented. This knowledge gap is due to insufficient data collection at low macroscopic stress levels, which results in a lack of information about the onset of deformation at BTGBs. In addition, the influence of microstructural features on their mechanical behavior remains poorly understood. For example, the consequences of a substantial misalignment between c-axes on either sides of the grain boundary, or the effect of the twist angle are unknown. This knowledge gap partly stems from the low density of these microstructure configurations [26,34], which implies a difficult analysis of a statistically significant number of instances. In this context, different influences of BTGB characteristics on deformation and cracking sensitivity remain to be clarified as well. Interestingly, cracks were previously identified at these microstructure configurations in a fracture toughness assessment framework [35]. While this observation suggests that BTGBs might be prone to cracking under monotonic loadings, no study of damage evolution at BTGBs was reported to the best of the authors' knowledge. Hence, it is not clear whether they are associated with the first cracks, and the

corresponding macroscopic strain level. In summary, essential information about the mechanical behavior of BTGBs remains missing to understand failure mechanisms in titanium alloys.

In this study, deformation and fracture at BTGBs was investigated in the Ti-6Al-4V alloy with a special emphasis on the influence of the features of the GB. An automated detection tool developed in a previous study was used alongside large scale electron back-scattered diffraction (EBSD) mapping to consider a population of BTGBs with different characteristics. Although significant deviations from a pure twist configurations were included in the analysis, investigated GBs are denoted as BTGBs throughout the article for clarity purposes. In situ scanning electron microscopy (SEM) tensile tests combined with high resolution digital image correlation (HR-DIC) were employed to extract quantitative information about the onset and the development of deformation at BTGBs. Monitoring was pursued until early cracking events occur at BTGBs to obtain insights into the fracture resistance, and the relation to prior deformation. Complementary atomistic simulations were carried out to identify the structure of BTGBs and clarify the origin of the influence of BTGB characteristics on their mechanical behavior.

Results

Grain-scale deformation mechanisms

Engineering stress – strain curves reconstructed from in-situ tensile tests are reported in Figure 1a. All specimens exhibited similar tensile behaviors. Thus, results extracted from the different tests were merged together for subsequent analysis. In addition, yielding was detected at ~ 830 MPa on average, which compares well with the value obtained during the conventional tensile tests (i.e., 857 MPa). DIC data was first employed to identify active slip systems unrelated to BTGBs in the 33 regions of interest (ROI) using the procedure detailed in Methods section. The distribution of intragranular slip events noticed at each step before yield detection is displayed in Figure 1b. No basal or prismatic slip was

observed before the 600 MPa step, which is about 72 % of the yield strength. Similar levels were reported in previous studies [27]. The onset of both slip modes occurred simultaneously. Different trends reported in prior studies might be related to the coarse load increments, which can hinder slightly shifted onset of slip activity, and texture, which can result in a different representation of the various slip systems [36,37]. A critical resolved shear stress (CRSS) value was computed considering a uniaxial tension global stress state. The resulting CRSS for basal slip is about 313±52 MPa, versus 315±50 MPa for prismatic slip. This assumption can introduce bias as it does not account for heterogeneous stress distribution in polycrystalline samples. However, estimates are generally consistent with values established using more accurate approaches as illustrated in a recent review [38]. A more restricted number of slip events appears associated with pyramidal slip activity, and occur at higher macroscopic stress levels.

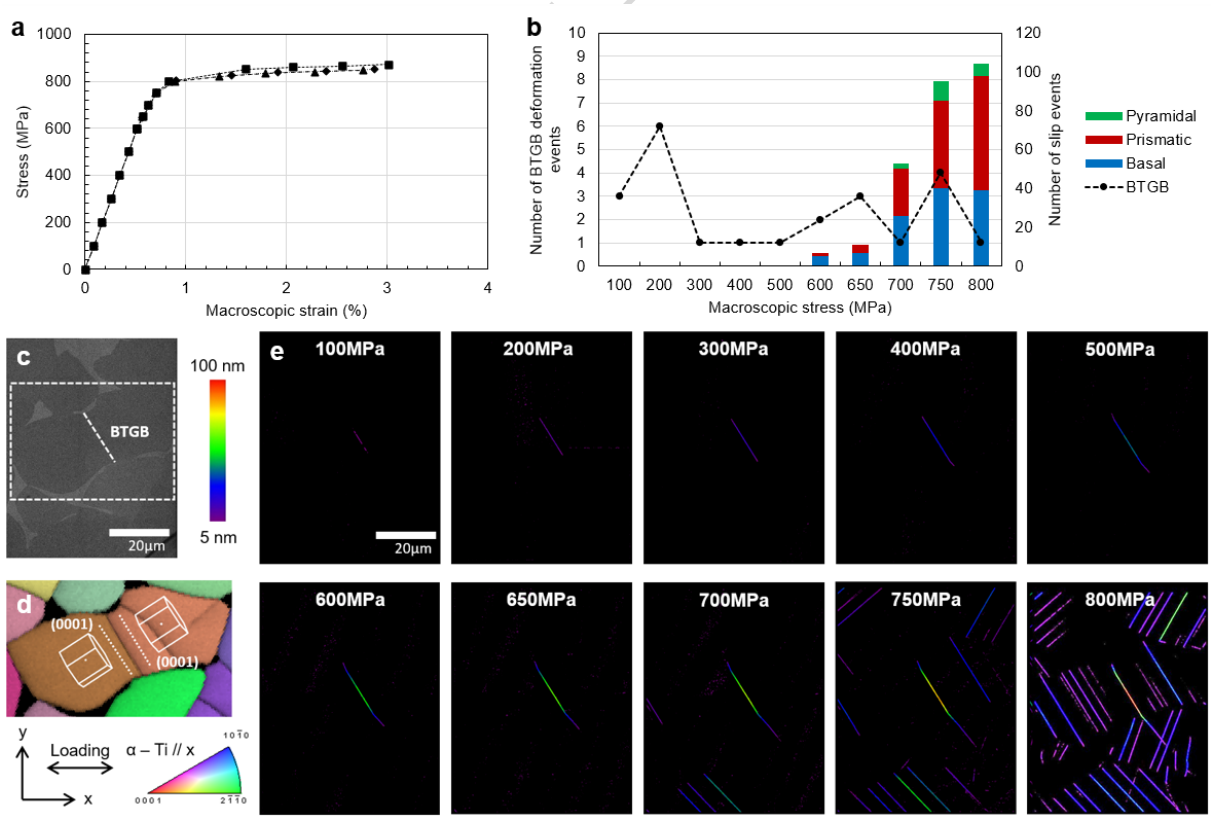

Figure 1: Plastic activity in the investigated Ti-6Al-4V alloy. a Reconstructed engineering stress – strain curves showing stops for all 3 in-situ tensile tests, **b** Distribution of plastic activity, showing intragranular slip events along basal, prismatic and pyramidal planes as well as shear along BTGBs, as a function of the macroscopic stress for all ROIs monitored during the experiments. A typical example of an early deformation event at a BTGB is illustrated in **c** to **e**. **c** SEM micrograph showing the microstructure surrounding a BTGB, **d** Inverse pole figure map superimposed with image quality indicating the crystal direction along the loading axis, and **e** In-plane slip magnitude maps showing the slip activity in the investigated region for different macroscopic stress levels.

Deformation events at BTGBs exhibited a different behavior. They were detected for macroscopic stress levels as low as 100 MPa, which is about 12 % of the yield strength. Consistently, the associated CRSS values are very low. They are reported in Supplementary Table 1. In particular, several occurrences lie in the 50 MPa – 100 MPa range, which is drastically lower than any value obtained for basal or prismatic slip. No monotonic increase in number of events per stress increment is observed, in contrast with conventional slip activity.

Characteristics of deformation at BTGBs

The sequence of deformation events in a ROI containing a BTGB prone to early deformation is exemplified in Figures 1c to 1e. Deformation at the BTGB was detected for a macroscopic stress as low as 100 MPa. No unrelated slip activity was detected until the macroscopic stress reached 700 MPa. This confirms that the first deformation events proceed at the BTGBs, and do not stem from slip activity in a neighboring region. Interestingly, deformation extended from the BTGB to the neighboring grain, starting from the 500 MPa step. At this step, no other intragranular slip trace was observed. This feature indicates an indirect role of BTGBs on triggering early intragranular slip activity. This phenomenon was frequently observed in the various ROIs. In particular, it occurred for a macroscopic stress level as low as 300 MPa, which is half the threshold stress for intragranular slip activity unrelated to a BTGB.

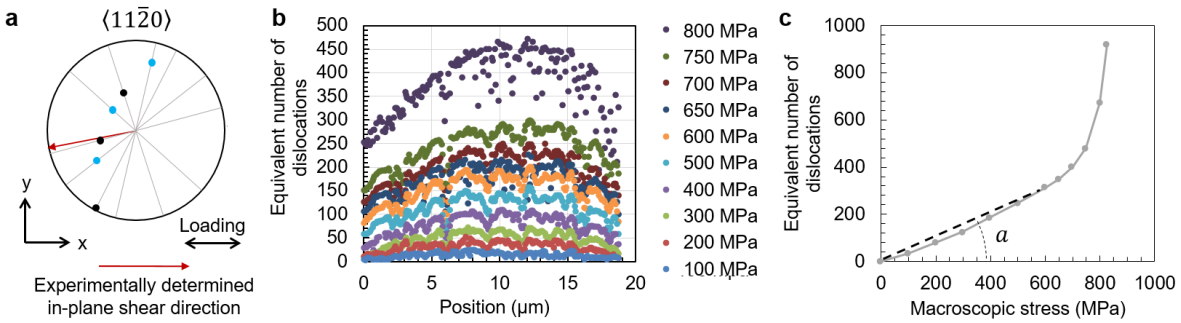

Figure 2: Characteristics of deformation events at BTGBs. a Pole figure showing <a> directions in α gains adjacent to the BTGB, and the experimentally determined in-plane shear direction. The loading direction is horizontal. **b** Profiles of equivalent number of dislocations calculated at the BTGB shown in Figure 1, and **c** Maximum value of the equivalent number of dislocations as a function of the macroscopic stress at the same location.

Quantitative information collected for each deformation event includes the in-plane slip direction. It was used in prior studies to determine the <a> slip direction for basal or prismatic slip [39,40]. A similar approach was applied to confirm that BTGB shear proceeds along a <a> direction. An example of analysis is reported in Figure 2a. The experimentally measured in-plane slip direction is shown. The 6 possible <a> directions pertaining to both adjacent α grains are also reported for comparison. For all BTGB deformation events, the in-plane projection of a <a> direction consistently matched the experimental in-plane slip direction. This feature indicates that BTGB deformation proceeds through shear along a <a> direction. It is worth noting that this result was used for the CRSS calculations reported in the previous paragraphs, as the identification of the plane and direction was needed. The identified slip direction was then used to calculate the equivalent number of dislocations resulting in the experimentally measured displacement as described in the Methods section. The profiles extracted from the BTGB deformation event shown in Figure 1e are displayed in Figure 2b. The parabolic evolution of the equivalent number of dislocations is typical of dislocation pile-ups against obstacles such as GBs [41]. The maximum value reached in the example of Figure 1e was extracted at each step, and reported in Figure 2c. The evolution with respect to the stress is linear in the macroscopic elastic regime, but a sharp

increase is observed upon extensive development of plastic deformation, which occurs for a macroscopic stress of $\sim 800\ MPa$.

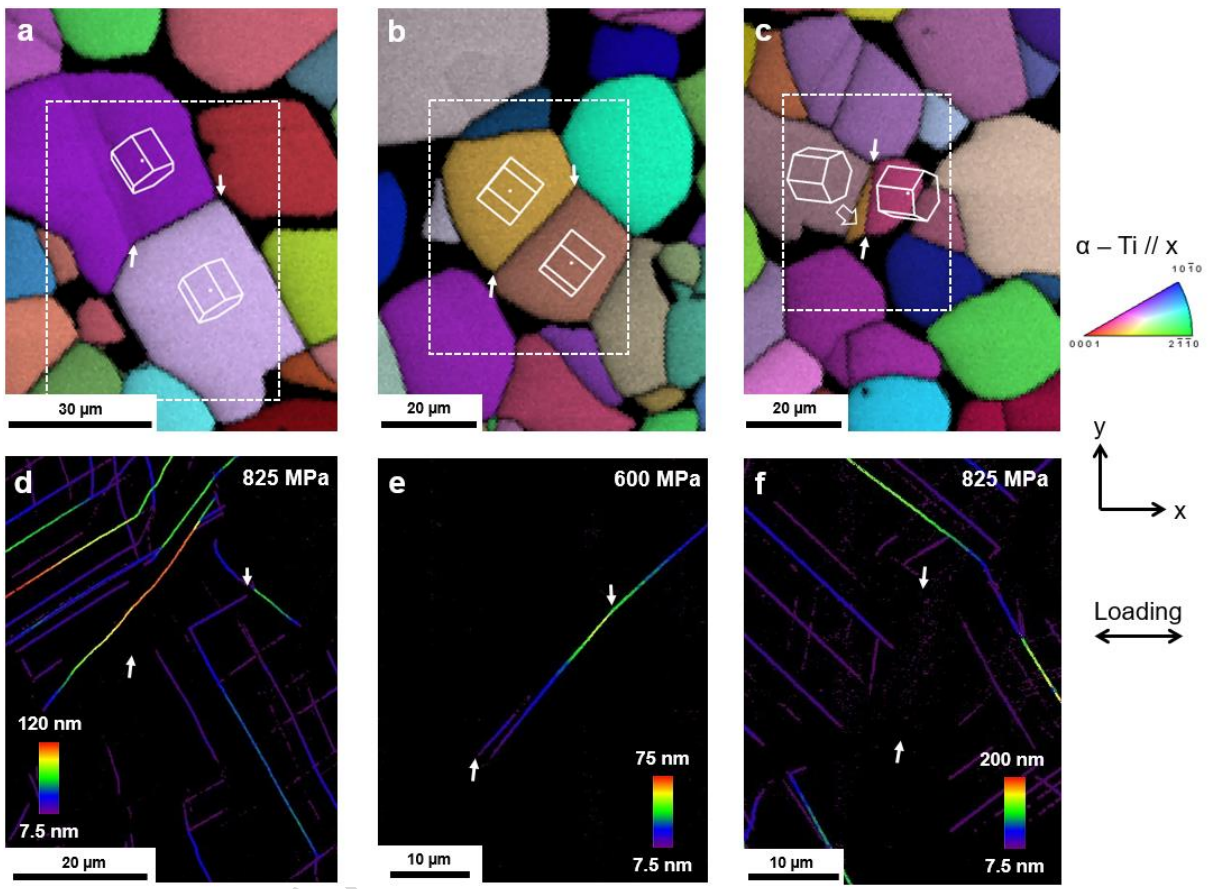

Figure 3: Examples of deformation events highlighting the variability in behavior observed at BTGBs. Inverse pole figure map superimposed with image quality showing the crystal direction along the loading axis **a**-**c**, and the corresponding in-plane slip magnitude map **d**-**f** for **a** and **d** BTGB shear concurrent with a prismatic slip event intersecting the GB, **b** and **e** Discontinuous BTGB deformation due to deviation of the GB plane from the basal planes, and **c** and **f** No deformation at the BTGB. White arrows indicate both ends of the BTGB.

As highlighted in the previous paragraphs, deformation events located at BTGBs often interact with intragranular slip events in the surrounding microstructure. Two BTGBs exhibited a late onset of deformation concurrent with the activation of prismatic or pyramidal <a> slip in adjacent α grains. Shearing was restricted to portions of the BTGBs intersected by the slip traces, and detected for a

macroscopic stress higher than 700 MPa. These GBs are indicated in Supplementary Table 1, and an example is shown in Figures 3a and 3d. Dislocations from the bulk might be absorbed and glide along BTGBs as previously observed at unspecified grain boundaries using transmission electron microscopy [42,43]. However, dislocation emission from GBs may also occur [44]. In addition, a GB classified as a BTGB but exhibiting a deviation from the basal plane in the center of the GB by a few degrees is shown in Figures 3b and 3e. Deformation occurs along a small portion of the BTGB on the right hand side of the micrographs, but switches to the basal plane upon deviation of the GB plane. Interestingly, BTGB shearing occasionally extended along curved GB segments as well, for minimal deviations from the basal planes. Finally an example of a BTGB resistant to deformation is shown in Figures 3c and 3f. These examples highlight the variety of behaviors observed in this study.

Influence of BTGB characteristics on deformation behavior

BTGB configurations in the investigated material span a wide range of characteristics, including misorientation angles, c-axes deviations, lengths, and BTGB orientations relative to the loading axis. This feature is highlighted in the statistical analysis of a reference BTGB population reported in Supplementary Note 1 and Supplementary Figure 1. The differences in behavior evidenced in the previous paragraphs were analyzed considering these characteristics. CRSS values measured at BTGBs are reported in Figure 4a as a function of the misorientation angle. Numerous values are lower than 100 MPa, and two lower than 50MPa. Regarding the BTGB misorientation, low CRSS values were obtained from approximately 10° to 30°. Error bars indicate no overlap with CRSS values for basal and prismatic slip. This feature unambiguously indicates a very different behavior. In contrast, misorientation angles lower than approximately 10° were associated with CRSS values higher than roughly 200 MPa. A significant transition in behavior is thus observed for this misorientation level (~ 10°). CRSS values are plotted as a function of the misorientation between the c-axes in Figure 4b. The lack of obvious trend highlights that significant deviations between c-axes on either sides of the BTGBs do not prevent low

stress deformation at BTGBs. CRSS values are plotted as a function of the BTGB length measured on the surface of the specimens in Figure 4c. No significant trend arises. The lack of information about the in-depth geometry of the BTGB may contribute to the insensitivity of the CRSS to the BTGB length measured on the surface of the specimen. CRSS values are plotted in Figure 4d as a function of the BTGB inclination relative to the loading direction. Low stress deformation at a BTGB was observed for values from 15° to 80°. This domain is larger than typically observed for basal slip (i.e., from 15° to 65° according to [37]). As the CRSS for deformation at BTGBs is very low, as compared to the CRSS for basal slip, it can proceed for orientations leading to low resolved shear stress.

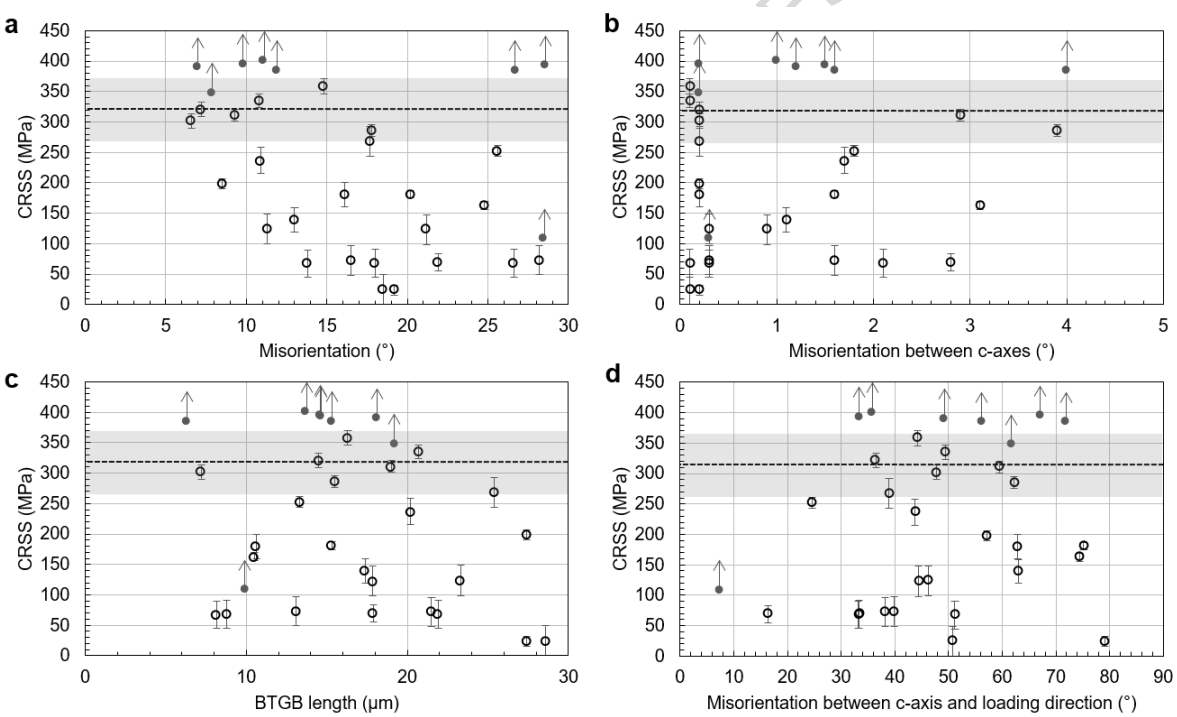

Figure 4: Relation between CRSS values and BTGB characteristics. CRSS values plotted as a function of **a** the misorientation at the BTGB, **b** the misorientation between c-axes on either side of the BTGB, **c** the BTGB length measured on the surface of the specimens, and **d** the misorientation between the c-axes and the loading direction. Empty symbols indicate the observation of shear along BTGBs, while full symbols indicate no shear at the last loading step. The mean CRSS for basal or prismatic slip is also shown by a dashed line with the standard deviation range in grey.

Origin of the influence of BTGB characteristics on deformation behavior

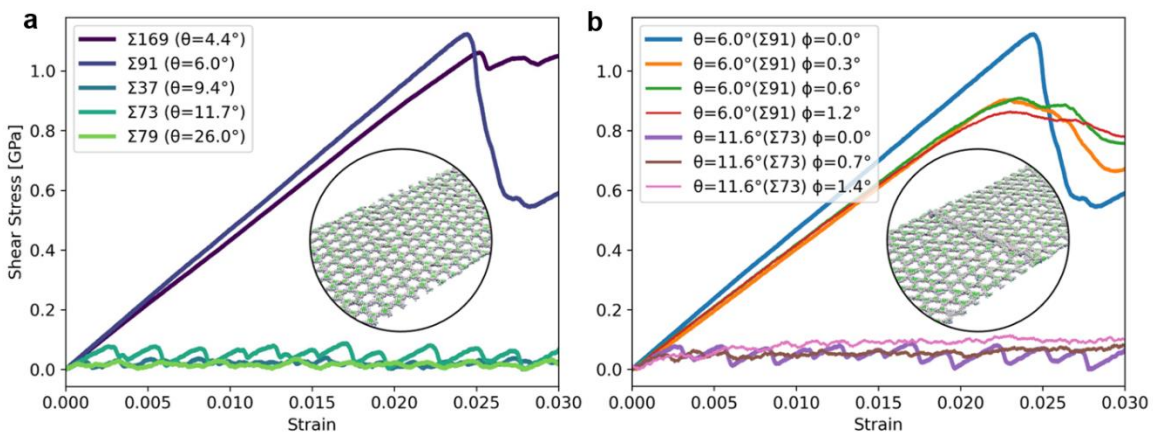

Figure 5: Shear of BTGBs at room temperature by molecular dynamics simulations. a Stress – strain curves of the shear stress response under shear strain for the Σ169, Σ91, Σ37, Σ73 and Σ79 BTGBs with misorientation angles of 4.4°, 6.0°, 9.4°, 11.6° and 26.0°, respectively. **b** Stress – strain curves for the Σ91 and Σ73 BTGBs with additional tilt angles ϕ. The 0° tilt angle correspond to the BTGB shown in **a**. Insets show the interfacial dislocation networks forming the GB as revealed by Common Neighbors Analysis.

The shear strength of different BTGB configurations was computed by molecular dynamics (MD) simulations to clarify the relation between BTGB characteristics and the mechanical response. Five BTGBs were selected to consider the full range of twist angles. Figure 5a shows the shear stress responses under shear strain at room temperature for the Σ169, Σ91, Σ37, Σ73 and Σ79 BTGBs with misorientation angles of 4.4°, 6.0°, 9.4°, 11.6° and 26.0°, respectively. The shear strengths, defined here as the maximum stress reached during the simulation, are listed in Supplementary Table 2. BTGBs with a misorientation angle lower than ~ 8 ° exhibit shear strengths around 1 GPa, while shear strengths were one order of magnitude lower for higher twist angles. Simulations revealed that the transition between two strength regimes occurs for angles between 6.0° and 9.4°. Interestingly, it is not associated with the low-/high-angle character of the BTGB, which transitions between 15° and 17°. Thus, the existence, or the lack, of GB dislocation networks cannot account for the large variation in strength.

The dislocation networks forming the low-angle BTGBs show substantial differences for twist angles lower or higher than ~ 8°. The interfacial dislocation networks at the Σ91 and Σ73 low-angle BTGBs are displayed in Figure 6 at 0 K and at 300 K. A distinctive triangular pattern with a characteristic size of a few nanometers is observed at 0 K. It is formed by three arrays of partial screw dislocations with the Burgers vectors $a_0/3\,[10\bar{1}0]$, $a_0/3\,[1\bar{1}00]$ and $a_0/3\,[01\bar{1}0]$. The dislocations spacing within an array being a function of the misorientation angle, the triangles forming the pattern are larger for the Σ91 than for the Σ73. Besides the spacing, there is however no other difference. At room temperature (i.e., 300 K), a triangular pattern with similar features was observed for the Σ73 BTGB, while a Kagome pattern was noticed for the Σ91 BTGB. A Kagome pattern was also observed for the lower-angle Σ169 BTGB. Pattern evolution results from thermally activated reorganization of the network, which consists in the motion of one of the dislocation arrays. As a consequence, simple coplanar dislocation junctions are formed instead of triple ones. This also modifies the stacking fault density at the interface, with a 55 % reduction for the Σ91 as an example. This feature is illustrated in Supplementary Figure 2. The driving force is the competition between the transformation of the triple junctions into simple junctions, the reduction of stacking faults density, and the stronger dislocation lines interactions. Note that, as this reorganization does not modify dislocation spacing, it has no consequence on the misorientation angle of the BTGB.

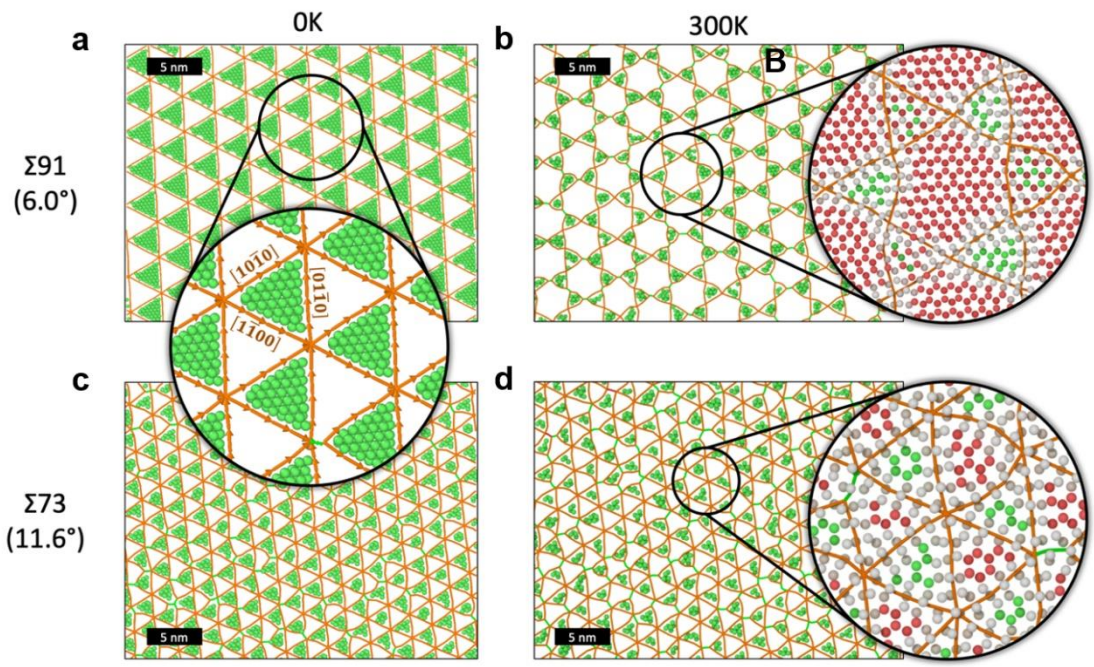

Figure 6: Interfacial dislocation network for different BTGB configurations. Images of the dislocation network at the Σ91 (**a** and **b**) and Σ73 (**c** and **d**) low-angle BTGBs at 0 K (**a** and **c**) and at 300 K (**b** and **d**). Partial and full dislocation lines are shown with orange and green lines, respectively, as obtained by Dislocation eXtraction Analysis. Atoms forming stacking faults (FCC environment) are shown in green, while other atoms are hidden. Insets show details of the interfacial dislocation network, including atoms in HCP environment within the two basal atomic planes forming the BTGB. Views are along the c axis.

The negligible influence of c-axes misalignment on the mechanical response is another salient observation from the experiments. In our atomistic samples, the introduction of edge dislocation arrays with various spacing resulted in different tilt angles, in addition to the main twist component. This feature is illustrated in Supplementary Figure 3. The shear stress responses under shear strain at room temperature are shown in Figure 5b for the Σ91 and Σ73 BTGBs with different tilt angles. For both twist angles, these results show that a small tilt component does not significantly change the mechanical response and, more importantly, the strength transition associated with the change of interfacial dislocation network pattern. The shear strengths are reported in Supplementary Table 2. As a side note,

the variations of elastic moduli for different twist and tilt angles originate from the well-known influence of dislocations type and density on the elastic response [45,46].

Fracture at BTGBs

Increasing the macroscopic strain in-situ in the SEM resulted in crack nucleation at BTGBs. An example is shown in Figure 7a and 7b. At a macroscopic strain of 1.46 % a crack is open along the BTGB where a step visible at a macroscopic strain of 0.91 % (i.e., the previous test interruption) is indicative of preliminary deformation. This observation confirms that displacements measured on the surface of the deformed sample using HR-DIC are not related to cracking, but deformation. Thus, the BTGBs do not exhibit a brittle behavior. All tensile tests were pursued until ~ 3 % strain as shown in Figure 1a. Over the 33 ROIs, 4 cracking events were noticed. They were detected at the 1.46 %, 1.92 %, 2.40 %, and 3.09 % strain steps, respectively. These observations reveal that cracks can nucleate at BTGBs for a monotonic tensile loading at low macroscopic strain. Also, unimpeded growth occurred along the whole BTGB segment during a single loading step. This feature highlights a low resistance to cracking. However, it was observed that crack extension generally stopped upon deviations from the basal planes, which corresponds to increasing GB curvature. This behavior is illustrated by the lack of cracking on the left hand side of the BTGB shown in Figure 7b, although a surface offset induced by deformation was observed at the previous step in Figure 7a. As a side note, the latter observation highlights that shearing can extend along GBs despite significant curvature at relatively high stress levels, in contrast with the behavior shown in Figures 3b and 3e.

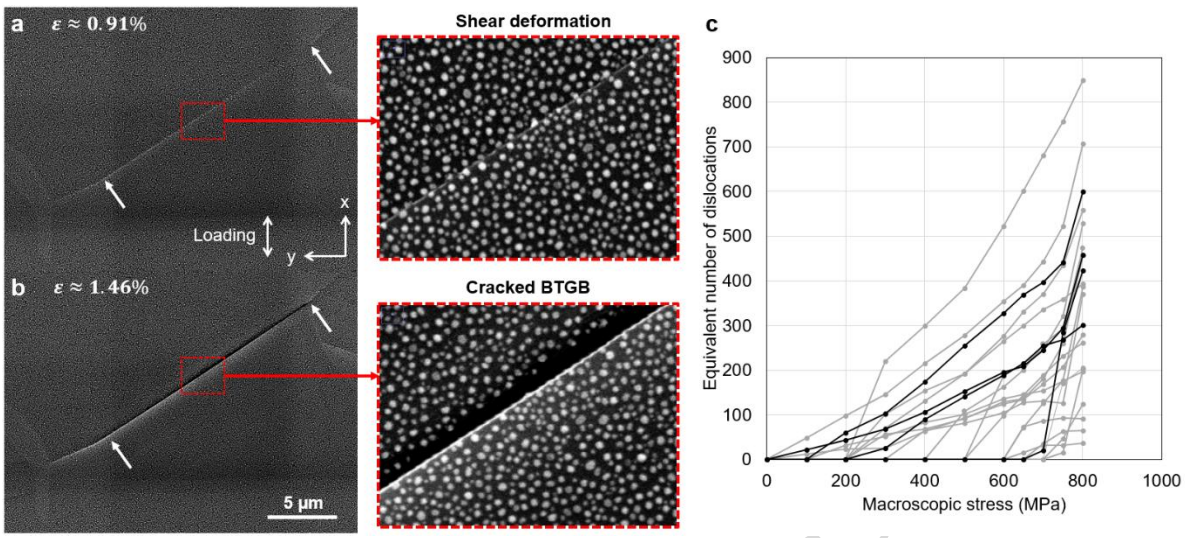

Figure 7: Transition from localized deformation to cracking at BTGBs. SEM micrographs showing a BTGB before (**a**), and after (**b**) cracking. White arrows indicate both ends of the BTGB. Round particles visible on the micrographs correspond to the gold speckle used for DIC. **c** Maximum equivalent number of dislocations plotted as a function of the macroscopic stress for all BTGBs. BTGBs prone to cracking are indicated in black, while the others are shown in grey. It is to be noted that cracking occurred at steps not shown in this plot.

All cracked BTGBs exhibited evidence of deformation prior to cracking. Thus, it appears as a required step. In contrast, no convincing evidence of a key role of an intragranular slip event intersecting the BTGB was obtained. DIC data was obtained in all ROIs until the yield strength was reached, and the equivalent number of dislocations was calculated to assess whether cracking was related to the magnitude of preliminary shearing along the BTGB. The maximum values are reported as a function of the macroscopic stress in Figure 7c for all considered BTGBs. Overall, the magnitude appears important. Cracked BTGBs exhibited an equivalent number of dislocations at the 800 MPa step higher than 39 % of overall BTGB population showing evidence of deformation. On average, the equivalent number of dislocations was 445 for cracked BTGBs, versus 343 for other BTGBs showing evidence of deformation at this step. However, several BTGBs associated with intense deformation did not experience cracking, and the equivalent number of dislocations fails at predicting the crack nucleation sequence (i.e., the higher

the number of dislocations, the earlier the occurrence of cracking). In particular, DIC analysis was achieved at the last step before cracking of BTGB L2-3 from test number 2. At this step, BTGB L1-6 from the same test had a higher equivalent number of dislocations, but remained uncracked. Also, as shown in the data reported in Supplementary Table 1, cracking is not correlated with an early onset of deformation at the BTGB, or a low CRSS value. For example, the BTGB L2-6 from test number 2 was associated with a CRSS of about 250 MPa and cracked before the end of the test, while BTGBs with CRSS values lower than 50 MPa did not.

Influence of BTGB characteristics on fracture

To clarify the differences in cracking resistance identified in the previous paragraph, the influence of BTGB features was investigated as previously carried out to analyze the onset of deformation. Distributions of the total number of BTGBs, the number of deformed BTGBs, and the number of cracked BTGBs are reported in Figure 8 as a function of misorientation angle at the BTGB (a), the misorientation between c-axes on either side of the BTGB (b), the BTGB length measured on the surface of specimens (c), and the inclination of the BTGB relative to the loading axis (d). Regarding the BTGB misorientation, the population of cracked BTGBs spans a wide range of values. Thus, no significant influence of the twist angle was identified. Similarly, the misalignment of c-axes on either side of the BTGB is not a critical feature regarding the cracking sensitivity of BTGBs. Indeed, cracking events follow the distribution obtained for deformation at BTGBs, which can occur for deviations up to a few degrees. No significant influence of the BTGB length was observed as well. In contrast, all BTGBs with c-axes inclined between 15° and 35° from the loading direction, and showing early deformation, were prone to cracking. Furthermore, no crack was noticed for values out of this range. This result suggests that the orientation of the BTGB relative to the loading axis is a critical feature for crack nucleation.

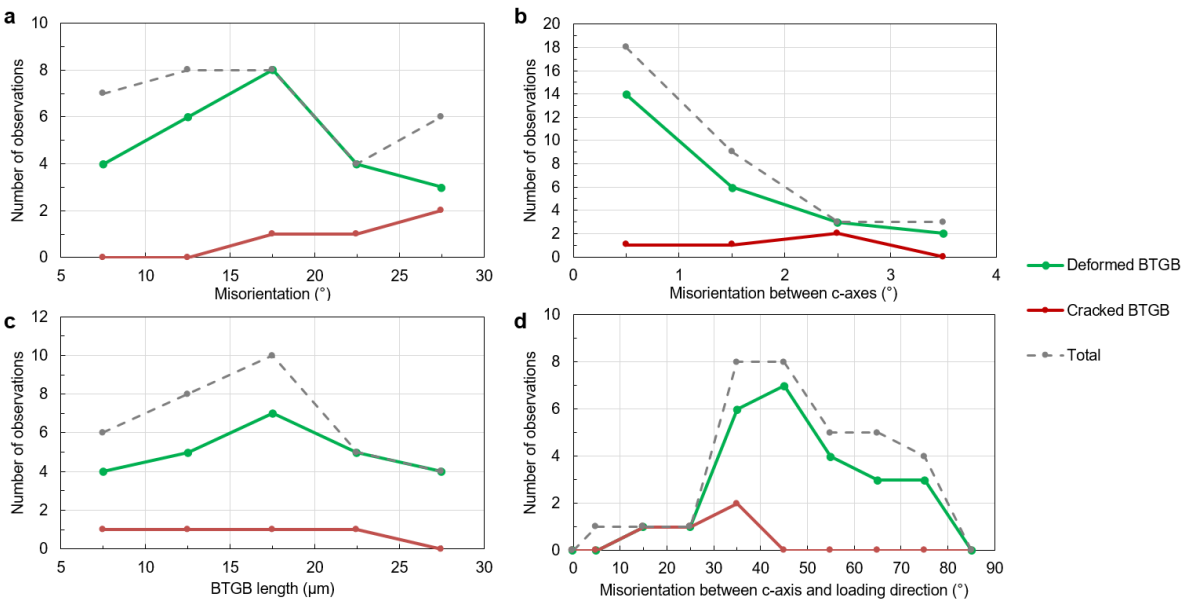

Figure 8: Relation between BTGB characteristics and cracking sensitivity. Number of considered BTGBs (total), deformed BTGBs, and cracked BTGBs plotted as a function of **a** the misorientation at the BTGB, **b** the misorientation between c-axes on either side of the GB, **c** the BTGB length measured on the surface of the specimen, and **d** the misorientation between the c-axis and the loading direction in α grains adjacent to the BTGB.

To confirm this hypothesis, automated SEM mapping of the entire regions considered in the large scale EBSD maps was carried out after the in-situ tests. In these locations, some BTGBs did not satisfy the presently used detection criteria, or were not selected as ROIs for in-situ monitoring, but might be prone to cracking. One additional crack was found. The BTGB misorientation was about 13.2°, c-axes were misaligned by about 0.3°, the inclination of the c-axes relative to the loading direction was 24.9°, and the BTGB length was approximately 8.6 µm. The low c-axis inclination confirms the importance of the orientation of the BTGB relative to the loading direction identified in the previous paragraph. The presence of no other crack demonstrates that BTGBs are preferred locations for early damage under monotonic loadings, and supports the relevance of detection criteria employed in this study.

Discussion

The in situ tensile experiments revealed an early onset of plastic deformation at BTGBs. Indeed, evidence of shearing along BTGBs was obtained at macroscopic stress as low as 100 MPa, which implies that it was triggered at even lower stress. Thus, BTGB deformation was observed at approximately 12 % of the yield strength, while intragranular <a> slip was only observed beyond 70 %. A prevalent role of stress concentrations at BTGBs can primarily be ruled out. First, the transversely isotropic behavior of the HCP lattice in the elastic regime precludes stress concentrations along BTGBs, which accommodate a c-axis rotation of HCP lattices. Second, local stress concentrations arising from adjacent microstructure elements would statistically promote intragranular slip events instead of shearing along BTGBs. The presently obtained CRSS estimates are then expected to reflect the strength difference for intragranular and intergranular deformation events. Indeed, CRSS values for BTGB deformation are often in the 50 – 100 MPa range, while they are generally higher than 300 MPa for basal and prismatic slip, in agreement with assessments from prior studies [30,31,37,47]. The low CRSS permits BTGB deformation events to occur in microstructure configurations unfavorable for intragranular basal slip, typically leading to low associated Schmid factors. Another consequence is the presence of stress concentrations near triple junctions involving a BTGB. Evidence was obtained that early basal or prismatic slip activity in adjacent α grains can ensue from low stress deformation at BTGBs. BTGBs can thus behave as a source for the development of plastic deformation throughout the microstructure. This behavior is only expected if sufficient geometric compatibility is available. Illustrative examples are shown in Figure 9. The geometric compatibility of deformation systems on either side of the GBs was assessed using the m' parameter [48]. Values close to 1 (i.e., 0.81 and 0.93 for Figures 9a and 9b, respectively) indicate configurations favorable for slip transfer [49,50].

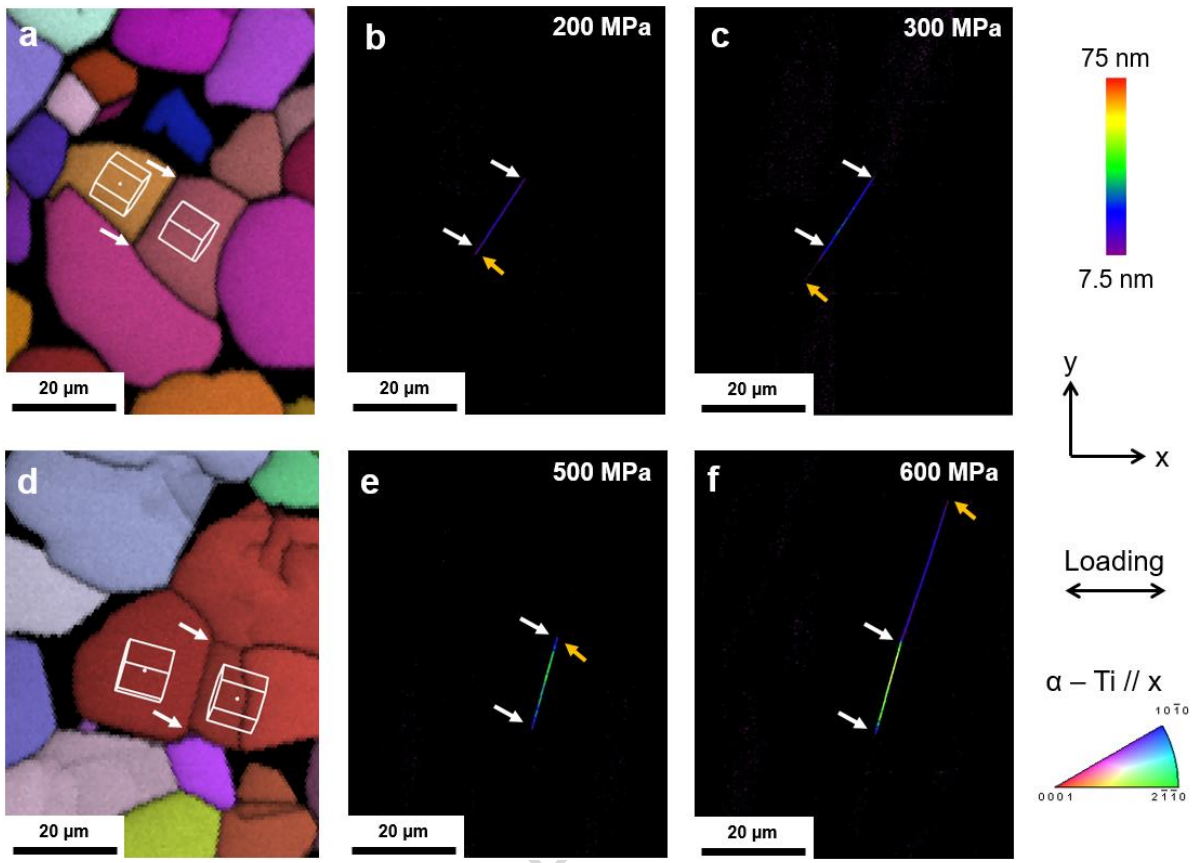

Figure 9: Examples of slip development from deformation events at BTGBs. Inverse pole figure maps superimposed with image quality showing the crystal direction along the loading axis in two ROIs containing a BTGB associated with deformation transfer to adjacent α grains (**a** and **d**). The corresponding in-plane slip magnitude maps are displayed for the onset of deformation (**b** and **e**), and deformation transfer (**c** and **f**). White arrows indicate both ends of the BTGB and the yellow arrow the tip of the extending slip trace.

The detailed analysis of DIC data provided additional information about deformation at BTGBs. The measured displacements were consistent with shearing along a <a> direction belonging to an adjacent α grain for all BTGBs associated with deformation. This feature highlights an anisotropic response in the BTGB plane. Also, the parabolic evolution of the displacement values along BTGBs is typical of dislocation pile-ups. Details of the mechanism governing the low stress deformation behavior are currently under investigation. The influence of microstructural features on the mechanical response was studied as well. A salient feature is the observation of low stress deformation events for twist angles

higher than ~10° only. Another interesting finding is the negligible influence of deviations between c-axes on either side of the GB by up to ~3°. Therefore, a small tilt component does not inhibit the low stress deformation of BTGBs, or induce a significant strengthening. Insights into the origins of the twist and tilt effects were presently obtained using MD simulations, and will be discussed in the following paragraphs. No meaningful trend was extracted regarding the influence of the BTGB length on the CRSS. However, measurements of the BTGB length on the specimen surface may not accurately reflect the BTGB area. The lack of apparent size effect should thus be taken with care. Also, BTGBs being shorter than the diameter of a significant fraction of α grains, the low strength exhibited at BTGBs cannot stem from a slip length or grain size effect only [51].

These findings provide new information about the relationships between deformation and microstructural features at BTGBs. However, the deformation behavior of BTGBs was associated with a significant scatter. Thus, any conclusion based on experimental data should stem from several observations to rule out the intrinsic variability of their microstructural features and behavior. Importantly, the current understanding remains insufficient to accurately predict CRSS values. This may suggest limitations in the detection of BTGBs using surface characterization. Indeed, the lack of information relative to the 3D geometry of the GB might be an important issue. However, most ROIs showed deformation at the GB, which suggests that all criteria for a BTGB were generally satisfied. In particular, approximately half the BTGBs with a misorientation higher than 10° were associated with a low CRSS value (i.e., lower than 200 MPa), which indicates reasonable accuracy of BTGB detection procedures using surface based characterization techniques. Nevertheless, the details of possible nanoscale defects cannot be captured, although they may significantly influence the mechanical response of BTGBs. Also, mechanical fields in the surrounding microstructure likely play an important role.

Further evidence of low-stress deformation at BTGBs was obtained from the MD simulations. This result confirms the strength difference for intragranular and intergranular deformation inferred from experiments, despite differences in applied strain rates. As a consequence, a minimal influence of thermally activated processes such as diffusion or dislocation climb is expected, which echoes with the insensitivity of the BTGB cracking mechanism to the loading frequency reported in prior studies. Importantly, simulations replicated the experimental behavior considering pure titanium and defect-free BTGBs. Solutes, and crystallographic defects such as vacancies or dislocations, present in microstructures of engineering materials are thus unlikely to be the main cause of the low-stress deformation behavior observed in experiments. A recent investigation revealed dislocation structures in a BTGB using transmission electron microscopy, which likely pertained to deviations from the pure twist configuration [52]. Simulations of mixed GBs with ~ 1° tilt components showed no significant influence on the mechanical behavior, in agreement with experimental observations. The present results reveal that limited consequences may be induced by small deviations from the pure twist configuration. However, the lack of cracks at BTGBs with tilt angles above 4° in the study by Bean et al. suggests that the low-stress deformation behavior may vanish beyond this value [26]. The rare experimental observations carried out for tilt angles exceeding ~3° in the present investigation are consistent with this trend. However, configurations with tilt components in the 3° - 4° range are relatively infrequent in the investigated material, as shown in Supplementary Figure 1, making experimental confirmation challenging.

Atomistic simulations also revealed a direct correlation between the strength of the BTGB and the type of interfacial dislocation network. High shear strengths are associated with Kagome patterns, while lower shear strengths are observed for triangular patterns. The stable coplanar dislocation junctions formed in the Kagome network appear to strengthen BTGBs as compared to the unfavorable and highly energetic coplanar triple-dislocation junctions formed in the triangular network. We expect the

differences in interfacial dislocation networks to govern the experimentally observed evolution of CRSS magnitudes with increasing twist angles. Threshold twist angles for the transition in mechanical response are ~ 8 ° and ~ 10 ° for simulations and experiments, respectively. A good agreement is thus obtained considering limitations of current approaches. Notably, the limited population of BTGBs, and the associated variability in mechanical behavior, result in an uncertainty of typically a few degrees. In addition, the annealing time accessible by MD is orders of magnitude lower than in experiments. Longer times at high temperature likely promote the formation of the Kagome network. Also, the complexity of experimental configurations is not entirely reproduced in the simulations. Preliminary results suggest that local disorder such as solutes or vacancies may favor the formation of the Kagome network.

Cracking of BTGBs was observed in situ during the tensile test. According to large area SEM mappings carried out at the end of the test, BTGBs are preferred sites for early cracking events. In particular, the first crack was detected for a macroscopic strain lower than 1.5 %. While BTGBs have been previously linked to failures under cyclic loadings [19,26], the present observations highlight that they are prone to cracking at low strain for monotonic loadings as well. This feature echoes with the internal cracks noticed at BTGBs in the study by Liu et al. [35]. Presently reported observations also show that cracking proceeds along the whole length of the BTGB in a single loading step, suggesting a cleavage-like process. However, only 4 BTGBs were associated with cracking among the 33 considered BTGBs. These infrequent events can be rationalized using the two-step scenario described in the following. All cracked BTGBs exhibited localized deformation at macroscopic stress below the yield stress. A similar observation was made during cyclic loadings in a prior study [18]. This suggests that preliminary deformation is a required step for crack nucleation (step 1), and confirms that BTGBs do not exhibit a brittle behavior. Hence, criteria for deformation discussed in previous paragraphs (e.g., a twist angle higher than ~10°) are also relevant for cracking. However, the magnitude of the shearing could not be directly linked to the occurrence of, and the macroscopic strain associated with, BTGB cracking.

Therefore, maximum shear stain criteria alone are unlikely to properly predict fracture at these microstructure configurations. The inclination of the BTGB normal relative to the loading axis appeared a highly influential feature as well. Indeed, it was comprised between 15° and 35° for all cracking events noticed in this study (i.e., for macroscopic plastic strain lower than 3 %). This observation suggests that, despite local deviations from the global stress state, the stress component normal to the BTGB plane also plays a critical role in the cracking process, while being unimportant for deformation. Crack opening (step 2) occurs provided this stress component is sufficiently high. In this two-step scenario, prior shearing is likely to induce a stress amplification phenomenon, allowing the stress level to exceed the threshold for BTGB cracking. Interestingly, the trends extracted from the restricted number of events monitored during the in-situ tensile experiment are supported by the similar characteristics of BTGBs cracked during cyclic loadings, and suggest similar mechanical drivers. In particular, fatigue indicator parameters (FIPs) involving both the shear strain and the stress component normal to the basal planes have been widely employed to predict fatigue crack nucleation in various alloys [6,53]. Additional investigations are on-going to further clarify the mechanistic basis for BTGB cracking in a fatigue framework.

Conclusions

In summary, deformation and fracture at BTGBs were investigated in an engineering relevant Ti-6Al-4V alloy with an equiaxed microstructure. In situ SEM tensile tests combined with HR-DIC and large area EBSD mappings were employed to consider a population of BTGBs with a wide range of features. Deformation at BTGBs can occur at very low macroscopic stress (< 100 MPa), below 20% of the yield strength. Most associated CRSS values are approximately in the 50 – 100 MPa range, as compared to 300 - 350 MPa for basal or prismatic slip. As a consequence, shearing along BTGBs can occur in

configurations very unfavorable for basal slip, and intragranular slip in neighboring α grains can be activated early as compared to slip events unrelated to BTGB deformation. Low stress deformation was confirmed using MD simulations at defect free pure titanium BTGBs. This highlights no critical role of solutes and crystallographic defects at the grain boundary in the specific deformation behavior of BTGBs. Both methods revealed that a twist angle higher than ~8-10° is required for low stress deformation to occur, while no such behavior was observed below. This transition originates from the geometry of the interfacial dislocation network. Kagome networks observed for twist angles lower than ~ 8° results in a high CRSS, while triangular networks found for higher twist angles leads to a low CRSS. The lack of any interfacial dislocation network, as observed in high-angle BTGBs, is associated with a low CRSS as well. In contrast, a misalignment of c-axes on either sides of the BTGB by a few degrees (i.e., a tilt component < 4°) has no significant influence on their behavior. In addition, evidence of BTGB fracture was obtained at low macroscopic strain under monotonic tension (i.e., < 2 %). Cleavage-like cracking occurred along the full length of the BTGB during a single loading step. They appear as the weakest microstructural configurations under monotonic loading. Preliminary deformation is required for cracking to occur along BTGBs. While intense shearing is necessary, its magnitude was insufficient to predict fracture. However, a successful identification of cracked BTGBs was achieved through also considering the inclination of the c-axis relative to the loading direction. This feature highlights the critical role of the stress component normal to the BTGB plane in triggering cracking.

Methods

Material

A Ti-6Al-4V alloy with a fully equiaxed microstructure was employed in the present study. The measured composition was 6.52% Al, 4.22% V, 0.14% Fe, 0.21% O, and balance Ti. Coarse equiaxed α grains

embedded in residual β phase were obtained using a two-steps heat treatment applied to a Ti-6Al-4V forging. The first step was a 1 hour annealing at 950°C (i.e., 50°C below the β transus) followed by cooling at a controlled rate of 0.1°C / min. The final step was a 1 hour annealing at 700°C followed by cooling at a controlled rate of 4°C / min. Following this treatment sequence, the average α grain diameter was about 19 µm. A SEM micrograph and an EBSD map showing the microstructure are displayed in Supplementary Figures 4a and 4b respectively. Tensile properties were assessed using an Instron 8862 universal testing machine equipped with an extensometer. A nominal strain rate of 10^{-4} s^{-1} was applied using displacement control. The yield strength determined for a 0.2% plastic strain offset was 857 MPa, the ultimate tensile strength was 912 MPa, and the elongation was 19.8%.

BTGB detection procedure

Large area EBSD mappings were carried out to locate BTGBs on the surface of tensile specimens. For this purpose, they were first ground using SiC paper with decreasing particle size until 4000 grade. Specimens were then applied rough polishing using a diamond suspension containing 9 µm particles, before final polishing using a 90:10 mixture of a colloidal solution containing 0.04 µm silica particles and hydrogen peroxide. A JEOL 6100 SEM equipped with an Hikari EBSD detector manufactured by EDAX was used for EBSD characterization The microscope was operated at 25 kV with a probe current about 5 nA. EBSD data was collected at a rate about 150 Hz using a 5 x 5 binning and a standard Hough indexation strategy. A hexagonal grid with a 0.7 µm step size was used for an accurate description of the GB geometry. A total area of 11.1 mm^2 was characterized on each of the 3 specimens using this procedure.

EBSD data was processed using an in-house Matlab program based on Mtex [54] to identify and locate BTGBs. Guidelines established from a statistical analysis of fatigue cracks were applied to identify BTGBs. Details of the program were reported in a previous article [26]. All α/α GBs were analyzed through the

following criteria. The deviation between c-axes on either side of the α/α GB must be below 4°. The product of the angles between the α/α GB trace and the in-plane projection of the c-axis in each adjacent grain must be higher than 2.25. The maximum value is approximately 2.47. Only BTGBs with a length higher than half the average α grain size were considered. This threshold allows to rule out small segments, which often pertain to non-planar GBs. Complementary SEM observations of selected BTGBs were carried out in back-scattered electron mode using a JEOL IT800 microscope. This procedure allowed to collect high resolution micrographs of BTGBs. Indeed, wavy GB traces or residual β phase located at the GB remained occasionally unnoticed using EBSD characterization due to the lower spatial resolution of large area mappings. The observation of these features resulted in the associated BTGBs to be ruled out of the analysis.

Most BTGBs considered in this study satisfy additional requirements to be candidates for fatigue crack initiation. The maximum Schmid factor for basal slip in α grains adjacent to BTGBs must be higher than 0.2, and the misorientation between the c-axes of HCP lattices and the loading direction must be comprised between 10° and 65°. Statistical information about the BTGB population satisfying these criteria in the large area EBSD mappings is reported in Supplementary Note 1 and Supplementary Figure 1. An example of a BTGB detected using this procedure is also shown in Supplementary Figures 4c and 4d. Most BTGBs considered in the in situ tensile tests were selected from this population. However, the criteria were extended for a restricted number of BTGBs to study the deformation behavior and the cracking resistance of other configurations. For this purpose, BTGBs with misorientation angles lower than 10°, c-axes misalignments up to 4°, and c-axes inclinations in the 5° - 80° range were included in the analysis. For clarity purposes, all GBs are referred to as BTGBs despite occasionally significant misalignments between c-axes, which imply deviations from a pure twist character. Features of all BTGBs monitored in-situ are summarized in Supplementary Table 1. 10 to 13 BTGBs were considered in each specimen. This allowed to keep a reasonable and comparable time for each test.

In-situ tensile testing and HR-DIC analysis of deformation events

A Newtec MT1000 tensile stage equipped with a 5 kN loadcell was used for in-situ tensile testing. 3 specimens with a gage length of 10 mm, a gage width of 3 mm, and a thickness of 1 mm were machined using electrical discharge machining. Both faces were ground using SiC paper with decreasing particle size until 4000 grade. One face was then applied rough polishing using a diamond suspension containing 9 µm particles, before final polishing using a 90:10 mixture of a colloidal solution containing 0.04 µm silica particles and hydrogen peroxide. A speckle was then prepared to enable high spatial resolution DIC analysis using SEM micrographs. This framework is also referred to as high-resolution DIC (HR-DIC). A 5 nm thick gold layer was deposited using a Cressington 208hr sputter coater operated with a current of 20 mA. It was then remodeled under water vapor for 1.5 h at 300 °C. The resulting average particle radius is about 16 nm.

Before tensile testing, all regions of interest (ROI) were mapped using a JEOL IT800 SEM in secondary electron mode. A 2 x 2 array of micrographs was centered on each BTGB to define ROIs. A 10 % overlap was applied for neighboring micrographs. Guidelines reported in prior studies were used to determine imaging conditions appropriate for DIC [55,56]. The accelerating voltage of the microscope was 15 kV and the probe current was set at 40. Micrographs with a resolution of 4608 x 3840 pixels² were acquired using a dwell time of 6 µs per pixel. Employed magnification settings resulted in a definition of 10 nm / pixel. Individual tiles were stitched using the "grid/collection stitching" routine implemented in the ImageJ software [57,58]. In situ tensile testing was achieved using crosshead displacement control. A nominal strain equivalent to 5×10^{-4} s^{-1} was applied using a crosshead displacement rate of 0.5 µm s^{-1}. The displacement was stopped manually at targeted macroscopic stress levels. Imaging of ROIs was repeated using the same procedure after a stress relaxation rate lower than 0.25 MPa/min was reached. Stops were carried out at similar macroscopic stress / strain levels for all 3 in situ tensile tests. HR-DIC analysis was performed for 100 MPa stress increments up to 600 MPa. Beyond, stops were achieved

using 50 MPa increments until yielding was detected on the recorded load - displacement data. As titanium alloys such as Ti-6Al-4V usually display a low strain hardening rate, the following steps were based on strain calculations. The displacement was increased in ~ 0.5 % strain increments, up to an additional 3 % strain after yielding.

Heaviside-DIC (H-DIC) was used in this study to characterize slip events. H-DIC is an extended version of the DIC method through the introduction of a Heaviside function in the subset shape function. Processing of SEM images within the HR-DIC framework was performed to quantitatively assess in-plane displacement discontinuities induced by slip events. Additional details about the method were reported in previous articles [59,60]. The subset size was 60 x 60 pixels² with a step size of 10 pixels. Error assessment revealed that in-plane displacements higher than 8 nm were successfully detected. In the present study, the magnitude and the direction of the in-plane displacement were employed to extract features of deformation events in the ROIs. The slip plane was determined through the comparison of the slip trace and the traces of basal, prismatic and first-order pyramidal planes. The associated slip direction was then identified by comparing the direction of the in-plane displacement computed using H-DIC with the in-plane projections of the <a> slip directions compatible with the identified slip plane, which were calculated from the EBSD data. Through this procedure, the active slip systems are completely determined. The magnitude of the in-plane displacement was then used to compute the equivalent number of dislocations resulting in the measured slip offset. For this purpose, local displacement values were divided by the in-plane projection of the identified Burgers vector.

Crack detection procedure

At the end of the in-situ tensile tests, cracks located out of ROIs were searched over the entire region associated with initial EBSD mappings. For this purpose, a Tescan Vega 3 SEM was operated using an automated mapping routine. ~ 1000 micrographs with a field of view about 200 µm were acquired in

back-scattered electron mode for each specimen. The speckle was removed beforehand to enable a reliable detection of microcracks. This was achieved through polishing the specimen surface for 5 minutes using a 90:10 mixture of a colloidal solution containing 0.04 µm silica particles and hydrogen peroxide.

Atomistic modelling

Atomistic samples of fully periodic BTGBs in Ti were prepared using Atomsk [61] according to the coincidence site lattice theory for HCP materials [62]. As representative systems, we constructed Σ169, Σ91, Σ37, Σ73 and Σ79 BTGBs with a misorientation angle θ of 4.4°, 6.0°, 9.4°, 11.6° and 26.0°, respectively. The details of each sample are presented in Supplementary Table 3. Minimization by molecular statics was performed by Conjugate Gradient (CG) and FIRE algorithms [63,64] as implemented in LAMMPS [65]. The interatomic interactions were described by a Modified Embedded Atom Method (MEAM) force field [66].

As illustrated in Supplementary Figure 5, we generated bicrystals with GBs located at Z=0 and Z=Z_{box}/2, with Z_{box} being the size of the simulation box along Z. A stress-free optimal GB configuration for a given misorientation was obtained after the optimization the microscopic degrees of freedom, as already extensively described in the literature [67–69]. This optimized GB structure was then brought to the thermal equilibrium at desired temperatures (300 K) and zero stress, in three steps: (i) attribution of atomic velocities following a Gaussian distribution equivalent to 600 K, (ii) equilibration within the microcanonical ensemble (NVE) for 30 ps, (iii) equilibration and relaxation of the residual internal stresses within the isothermal-isobaric ensemble (NPT) at 300 K and 0.0 Pa for 20 ps. The mechanical shear tests were conducted on these equilibrated systems by applying the shear strain γ_{yz}, within the NPT ensemble at 300 K, and a strain rate of 10^8 s^{-1} (Supplementary Figure 5b). More precisely, the entire simulation box was sheared in the Y direction on the XY plane, the Z direction corresponding to the c-

[0001] crystallographic direction of the samples. All the molecular dynamics simulations have been performed with time step of 1 fs and a Velocity-Verlet time integration scheme as implemented in LAMMPS [65].

Complementarily, we constructed Σ91 and Σ73 BTGBs with additional tilt components ϕ of 0.3°, 0.6°, 1.2° and 0.7°, 1.4°, respectively. The values of the ϕ angles are related to the length along Y of the simulation box, as periodic boundary conditions are still enforced for these mixed GBs. Supplementary Figures 3 and 6 illustrate the resulting mixed GBs.

The atomistic configurations were visualized and analyzed using Ovito [70]. Atoms were classified and colored according to the adaptive common neighbor analysis (aCNA) classification: red, green and white for atoms within an HCP, FCC and other crystallographic environment. Note that within an HCP crystal, stacking faults appears as FCC. aCNA is often referred to as CNA for simplicity. Dislocation lines and Burgers vectors were extracted from the atomistic configurations via the dislocation extraction algorithm (DXA) as implemented in Ovito.

Data availability statement

The datasets generated during and/or analyzed during the current study are available from the corresponding author, Samuel Hemery (samuel.hemery@ensma.fr), on reasonable request.

References

1. Gerd Lütjering, James C. Williams. *Titanium*. (Springer Berlin, Heidelberg, 2007).

2. Peters, M., Kumpfert, J., Ward, C. H. & Leyens, C. Titanium Alloys for Aerospace Applications. in *Titanium and Titanium Alloys* 333–350 (John Wiley & Sons, Ltd, 2005). doi:10.1002/3527602119.ch13.
3. Williams, J. C. & Starke, E. A. Progress in structural materials for aerospace systems1. *Acta Materialia* **51**, 5775–5799 (2003).
4. Peters, M., Hemptenmacher, J., Kumpfert, J. & Leyens, C. Structure and Properties of Titanium and Titanium Alloys. in *Titanium and Titanium Alloys* 1–36 (John Wiley & Sons, Ltd, 2005). doi:10.1002/3527602119.ch1.
5. Williams, J. C. & Boyer, R. R. Opportunities and Issues in the Application of Titanium Alloys for Aerospace Components. *Metals* **10**, 705 (2020).
6. McDowell, D. L. & Dunne, F. P. E. Microstructure-sensitive computational modeling of fatigue crack formation. *International Journal of Fatigue* **32**, 1521–1542 (2010).
7. Ozturk, D., Pilchak, A. L. & Ghosh, S. Experimentally validated dwell and cyclic fatigue crack nucleation model for α–titanium alloys. *Scripta Materialia* **127**, 15–18 (2017).
8. Xu, Y. *et al.* Predicting dwell fatigue life in titanium alloys using modelling and experiment. *Nature Communications* **11**, 5868 (2020).
9. Christ, H.-J., Fritzen, C.-P. & Köster, P. Micromechanical modeling of short fatigue cracks. *Current Opinion in Solid State and Materials Science* **18**, 205–211 (2014).
10. Lütjering, G. Influence of processing on microstructure and mechanical properties of (α+β) titanium alloys. *Materials Science and Engineering: A* **243**, 32–45 (1998).
11. Briffod, F., Shiraiwa, T., Enoki, M. & Emura, S. Effect of macrozones on fatigue crack initiation and propagation mechanisms in a forged ti-6Al-4V alloy under fully-reversed condition. *Materialia* **22**, 101401 (2022).

12. Bridier, F., Villechaise, P. & Mendez, J. Slip and fatigue crack formation processes in an α/β titanium alloy in relation to crystallographic texture on different scales. *Acta Materialia* **56**, 3951–3962 (2008).
13. Pilchak, A. L. & Williams, J. C. Observations of Facet Formation in Near-α Titanium and Comments on the Role of Hydrogen. *Metall Mater Trans A* **42**, 1000–1027 (2011).
14. Pilchak, A. L., Williams, R. E. A. & Williams, J. C. Crystallography of Fatigue Crack Initiation and Growth in Fully Lamellar Ti-6Al-4V. *Metall Mater Trans A* **41**, 106 (2009).
15. Bantounas, I., Dye, D. & Lindley, T. C. The effect of grain orientation on fracture morphology during high-cycle fatigue of Ti–6Al–4V. *Acta Materialia* **57**, 3584–3595 (2009).
16. Tympel, P. O., Lindley, T. C., Saunders, E. A., Dixon, M. & Dye, D. Influence of complex LCF and dwell load regimes on fatigue of Ti–6Al–4V. *Acta Materialia* **103**, 77–88 (2016).
17. Sinha, V. *et al.* Correlating Scatter in Fatigue Life with Fracture Mechanisms in Forged Ti-6242Si Alloy. *Metall Mater Trans A* **49**, 1061–1078 (2018).
18. Lavogiez, C., Hémery, S. & Villechaise, P. On the mechanism of fatigue and dwell-fatigue crack initiation in Ti-6Al-4V. *Scripta Materialia* **183**, 117–121 (2020).
19. Hémery, S. *et al.* Strain localization and fatigue crack formation at (0001) twist boundaries in titanium alloys. *Acta Materialia* **219**, 117227 (2021).
20. Lavogiez, C., Dureau, C., Nadot, Y., Villechaise, P. & Hémery, S. Crack initiation mechanisms in Ti-6Al-4V subjected to cold dwell-fatigue, low-cycle fatigue and high-cycle fatigue loadings. *Acta Materialia* **244**, 118560 (2023).
21. Hémery, S., Bertheau, D. & Hamon, F. Microtexture effects on fatigue and dwell-fatigue lifetimes of Ti-6Al-4V. *International Journal of Fatigue* **179**, 108068 (2024).
22. IOM3. Chapter 4: C-M-P – Deformation Behaviour . *F1000Research* **13**, 1189 (2024).

23. Wu, Z. *et al.* Crack initiation mechanism in a high-strength Ti-5Al-7.5V alloy subjected to high cycle fatigue loading. *Engineering Failure Analysis* **148**, 107201 (2023).
24. Liu, C. *et al.* Microstructural effects on fatigue crack initiation mechanisms in a near-alpha titanium alloy. *Acta Materialia* **253**, 118957 (2023).
25. Jia, R. *et al.* Crack nucleation and dislocation activities in titanium alloys with the strong transverse texture: Insights for enhancing dwell fatigue resistance. *International Journal of Plasticity* **175**, 103938 (2024).
26. Bean, C. *et al.* Microstructural statistics for low-cycle fatigue crack initiation in α+β titanium alloys: A microstructure based RVE assessment. *International Journal of Fatigue* **176**, 107854 (2023).
27. Hémery, S., Naït-Ali, A., Smerdova, O. & Tromas, C. Deformation mechanisms in the α phase of the Ti-6Al-2Sn-4Zr-2Mo titanium alloy: In situ experiments and simulations. *International Journal of Plasticity* **175**, 103947 (2024).
28. Pagan, D. C. *et al.* Modeling slip system strength evolution in Ti-7Al informed by in-situ grain stress measurements. *Acta Materialia* **128**, 406–417 (2017).
29. Williams, J. C., Baggerly, R. G. & Paton, N. E. Deformation behavior of HCP Ti-Al alloy single crystals. *Metall Mater Trans A* **33**, 837–850 (2002).
30. Jones, I. P. & Hutchinson, W. B. Stress-state dependence of slip in Titanium-6Al-4V and other H.C.P. metals. *Acta Metallurgica* **29**, 951–968 (1981).
31. Dawson, P. R., Boyce, D. E., Park, J.-S., Wielewski, E. & Miller, M. P. Determining the strengths of HCP slip systems using harmonic analyses of lattice strain distributions. *Acta Materialia* **144**, 92–106 (2018).
32. Zhang, Z., Jun, T.-S., Britton, T. B. & Dunne, F. P. E. Determination of Ti-6242 α and β slip properties using micro-pillar test and computational crystal plasticity. *Journal of the Mechanics and Physics of Solids* **95**, 393–410 (2016).

33. Hasija, V., Ghosh, S., Mills, M. J. & Joseph, D. S. Deformation and creep modeling in polycrystalline Ti–6Al alloys. *Acta Materialia* **51**, 4533–4549 (2003).

34. Lavogiez, C., Dureau, C., Nadot, Y., Villechaise, P. & Hémery, S. Crack initiation mechanisms in Ti-6Al-4V subjected to cold dwell-fatigue, low-cycle fatigue and high-cycle fatigue loadings. *Acta Materialia* **244**, 118560 (2023).

35. Liu, Y. *et al.* Discovery via Integration of Experimentation and Modeling: Three Examples for Titanium Alloys. *JOM* **67**, 164–178 (2015).

36. Echlin, M. P., Stinville, J. C., Miller, V. M., Lenthe, W. C. & Pollock, T. M. Incipient slip and long range plastic strain localization in microtextured Ti-6Al-4V titanium. *Acta Materialia* **114**, 164–175 (2016).

37. Hémery, S., Dang, T., Signor, L. & Villechaise, P. Influence of Microtexture on Early Plastic Slip Activity in Ti-6Al-4V Polycrystals. *Metall Mater Trans A* **49**, 2048–2056 (2018).

38. Hémery, S., Villechaise, P. & Banerjee, D. Microplasticity at Room Temperature in α/β Titanium Alloys. *Metall Mater Trans A* **51**, 4931–4969 (2020).

39. Chen, Z. & Daly, S. H. Active Slip System Identification in Polycrystalline Metals by Digital Image Correlation (DIC). *Exp Mech* **57**, 115–127 (2017).

40. Xu, X. *et al.* Identification of active slip mode in a hexagonal material by correlative scanning electron microscopy. *Acta Materialia* **175**, 376–393 (2019).

41. Sperry, R. *et al.* Slip band characteristics in the presence of grain boundaries in nickel-based superalloy. *Acta Materialia* **193**, 229–238 (2020).

42. Lee, T. C., Robertson ,I. M. & and Birnbaum, H. K. TEM in situ deformation study of the interaction of lattice dislocations with grain boundaries in metals. *Philosophical Magazine A* **62**, 131–153 (1990).

43. Joseph, S., Lindley, T. C. & Dye, D. Dislocation interactions and crack nucleation in a fatigued near-alpha titanium alloy. *International Journal of Plasticity* **110**, 38–56 (2018).

44. Murr, L. E. Strain-induced dislocation emission from grain boundaries in stainless steel. *Materials Science and Engineering* **51**, 71–79 (1981).

45. Koehler, J. S. & deWit, G. Influence of Elastic Anisotropy on the Dislocation Contribution to the Elastic Constants. *Phys. Rev.* **116**, 1121–1125 (1959).

46. Dokkum, J. S. V., Bos, C., Offerman, S. E. & Sietsma, J. Influence of dislocations on the apparent elastic constants in single metallic crystallites: an analytical approach. *Materialia* **20**, 101178 (2021).

47. Stapleton, A. M. *et al.* Evolution of lattice strain in Ti–6Al–4V during tensile loading at room temperature. *Acta Materialia* **56**, 6186–6196 (2008).

48. Luster, J. & Morris, M. A. Compatibility of deformation in two-phase Ti-Al alloys: Dependence on microstructure and orientation relationships. *Metall Mater Trans A* **26**, 1745–1756 (1995).

49. Hémery, S., Nizou, P. & Villechaise, P. In situ SEM investigation of slip transfer in Ti-6Al-4V: Effect of applied stress. *Materials Science and Engineering: A* **709**, 277–284 (2018).

50. Han, S. & Crimp, M. A. ECCI analysis of shear accommodations at grain boundaries in commercially pure alpha titanium. *International Journal of Plasticity* **131**, 102731 (2020).

51. Wang, L. *et al.* Direct measurement of critical resolved shear stress of prismatic and basal slip in polycrystalline Ti using high energy X-ray diffraction microscopy. *Acta Materialia* **132**, 598–610 (2017).

52. Wu, Z. *et al.* Preferential fatigue cracking at basal twist grain boundary (BTGB) in bimodal Ti-5Al-4V alloy: Dislocation activities and crack initiation. *Journal of Materials Science & Technology* **217**, 281–295 (2025).

53. Przybyla, C. P. & McDowell, D. L. Microstructure-sensitive extreme-value probabilities of high-cycle fatigue for surface vs. subsurface crack formation in duplex Ti–6Al–4V. *Acta Materialia* **60**, 293–305 (2012).

54. Bachmann, F., Hielscher, R. & Schaeben, H. Texture Analysis with MTEX – Free and Open Source Software Toolbox. *Solid State Phenomena* **160**, 63–68 (2010).

55. Stinville, J. C. *et al.* Sub-Grain Scale Digital Image Correlation by Electron Microscopy for Polycrystalline Materials during Elastic and Plastic Deformation. *Exp Mech* **56**, 197–216 (2016).

56. Kammers, A. D. & Daly, S. Digital Image Correlation under Scanning Electron Microscopy: Methodology and Validation. *Exp Mech* **53**, 1743–1761 (2013).

57. Schindelin, J. *et al.* Fiji: an open-source platform for biological-image analysis. *Nat Methods* **9**, 676–682 (2012).

58. Preibisch, S., Saalfeld, S. & Tomancak, P. Globally optimal stitching of tiled 3D microscopic image acquisitions. *Bioinformatics* **25**, 1463–1465 (2009).

59. Bourdin, F. *et al.* Measurements of plastic localization by heaviside-digital image correlation. *Acta Materialia* **157**, 307–325 (2018).

60. Valle, V., Hedan, S., Cosenza, P., Fauchille, A. L. & Berdjane, M. Digital Image Correlation Development for the Study of Materials Including Multiple Crossing Cracks. *Exp Mech* **55**, 379–391 (2015).

61. Hirel, P. Atomsk: A tool for manipulating and converting atomic data files. *Computer Physics Communications* **197**, 212–219 (2015).

62. Warrington, D. H. THE COINCIDENCE SITE LATTICE (CSL) AND GRAIN BOUNDARY (DSC) DISLOCATIONS FOR THE HEXAGONAL LATTICE. *J. Phys. Colloques* **36**, C4-95 (1975).

63. Bitzek, E., Koskinen, P., Gähler, F., Moseler, M. & Gumbsch, P. Structural Relaxation Made Simple. *Phys. Rev. Lett.* **97**, 170201 (2006).

64. Guénolé, J. *et al.* Assessment and optimization of the fast inertial relaxation engine (fire) for energy minimization in atomistic simulations and its implementation in lammps. *Computational Materials Science* **175**, 109584 (2020).

65. Thompson, A. P. *et al.* LAMMPS - a flexible simulation tool for particle-based materials modeling at the atomic, meso, and continuum scales. *Computer Physics Communications* **271**, 108171 (2022).
66. Kim, Y.-K., Kim, H.-K., Jung, W.-S. & Lee, B.-J. Atomistic modeling of the Ti–Al binary system. *Computational Materials Science* **119**, 1–8 (2016).
67. Symmetric and asymmetric tilt grain boundary structure and energy in Cu and Al (and transferability to other fcc metals) | Integrating Materials and Manufacturing Innovation. https://link.springer.com/article/10.1186/s40192-015-0040-1.
68. Wang, J. & Beyerlein, I. J. Atomic structures of symmetric tilt grain boundaries in hexagonal close packed (hcp) crystals. *Modelling Simul. Mater. Sci. Eng.* **20**, 024002 (2012).
69. Wang, H., Guénolé, J., Korte-Kerzel, S., Al-Samman, T. & Xie, Z. Defects in magnesium and its alloys by atomistic simulation: Assessment of semi-empirical potentials. *Computational Materials Science* **240**, 113025 (2024).
70. Stukowski, A. Visualization and analysis of atomistic simulation data with OVITO–the Open Visualization Tool. *Modelling Simul. Mater. Sci. Eng.* **18**, 015012 (2009).

Acknowledgements

The ANR (Agence Nationale de la Recherche) is gratefully acknowledged for funding this study: ANR-20-CE08-0006 (PLASLOTI) and ANR-21-CE08-0001 (ATOUUM). High Performance Computing resources were provided by the EXPLOR center of the Université de Lorraine and by GENCI at TGCC (Grants 2023-A0150914654 and 2024-A0170914654).

Author contributions

Conceptualization: JG, SH

Methodology: TY, DI, FH, JG, VV, SH

Investigation: TY, DI, JG, SH

Visualization: TY, DI, JG, SH

Supervision: VV, JG, SH

Writing—original draft: TY, SH

Writing—review & editing: TY, DI, FH, VV, JG, SH

Competing Interests statement

The authors declare that they have no competing interests.

Materials & Correspondence

Correspondence and material requests should be addressed to Samuel Hemery (samuel.hemery@ensma.fr) and Julien Guénolé (julien.guenole@cnrs.fr).

Editorial summary:

Basal twist grain boundaries in titanium alloys were recently identified as key microstructure configurations that lead to mechanical failures in service. This study examines deformation and fracture in these specific locations to shed light on the mechanical behavior in relation to grain boundary characteristics.

Peer review information:

Communications Materials thanks Zixu Guo and the other, anonymous, reviewers for their contribution to the peer review of this work.